ROYAL SOCIETY
OF CHEMISTRY

PAPER

Check for updates

A vibrating capillary for ultrasound rotation manipulation of zebrafish larvae†

Zhiyuan Zhang, [iD] [a] Yilin Cao,[a] Sara Caviglia,[b] Prajwal Agrawal, [iD] [a] Stephan C. F. Neuhauss[b] and Daniel Ahmed*[a]

Multifunctional micromanipulation systems have garnered significant attention due to the growing interest in biological and medical research involving model organisms like zebrafish (*Danio rerio*). Here, we report a novel acoustofluidic rotational micromanipulation system that offers rapid trapping, high-speed rotation, multi-angle imaging, and 3D model reconstruction of zebrafish larvae. An ultrasound-activated oscillatory glass capillary is used to trap and rotate a zebrafish larva. Simulation and experimental results demonstrate that both the vibrating mode and geometric placement of the capillary contribute to the developed polarized vortices along the long axis of the capillary. Given its capacities for easy-to-operate, stable rotation, avoiding overheating, and high-throughput manipulation, our system poses the potential to accelerate zebrafish-directed biomedical research.

Introduction

Zebrafish exhibit significant physiological and genetic parallels to humans, sharing common functional features with us and other mammals.[1–4] They have been pivotal in genetic screenings to identify mutant phenotypes mirroring human clinical conditions such as heart disease, various anemias, cancer, and neurological disorders. As such, zebrafish are also a crucial model for probing complex brain disorders. Zebrafish larval models serve as high-throughput and cost-effective alternatives in drug screening processes and are frequently used to elucidate the molecular mechanisms that underlie human diseases and identify treatments.[5–10]

Rotational manipulation of zebrafish larvae is a crucial capability to extract valuable anatomical information and achieve multidimensional analysis. As zebrafish become more central to research, the shortcomings of traditional handling platforms are evident, especially for tasks requiring high-throughput manipulation. The current practices—using agarose/gel[11,12] for mounting and fixation—are not only labor-intensive but also pose a risk of injury or death to the delicate larvae. Optical tweezers have been introduced to manipulate micro-objects[13,14] and organs[15,16] inside the body of a zebrafish larva, offering high precision but limited by a small operational area and shallow penetration depth, restricting their ability to handle the entire fish. Magnetic fields have also been utilized to rotate embryos by pre-injecting magnetic particles into the chorion, however, this method will inherently become ineffective when the embryos hatch from the chorion around two days post fertilization (dpf).[17] Managing the rotation of the slender body of a larva remains a significant challenge. To address this challenge, numerous automated zebrafish screening platforms have been created;[18–20] yet, these methods often restrict the larva to an enclosed space, hindering direct-contact and three-dimensional downstream treatments like micro-injection, mechanical analysis, and surface examination. Moreover, these platforms are inadequate to operate multiple zebrafish simultaneously.[21–23] Therefore, developing a multifunctional manipulation and analysis system remains key to accelerating zebrafish-directed biomedical research.

In contrast, ultrasound is an attractive modality to manipulate micro-objects with distinct advantages of biocompatibility, deeper penetration, no requirement for special sample properties (conductivity, transparency, and more), and the ability to generate large forces.[24–38] Currently, ultrasound-driven manipulation, in terms of trapping and rotating, has been achieved for microbeads,[39–43] cells,[44–50] and plant seeds,[51,52] by using surface acoustic waves and microbubbles. However, most of these subjects have nearly spherical structures with good symmetry and are ~5–100 μm in size; only a few work to date has been conducted on model organisms with

[a] *Acoustic Robotics Systems Laboratory, Institute of Robotics and Intelligent Systems, Department of Mechanical and Process Engineering, ETH Zurich, Säumerstrasse 4, CH-8803 Zurich, Switzerland. E-mail: dahmed@ethz.ch*
[b] *Neuhauss Laboratory, Department of Molecular Life Sciences, University of Zurich, Winterthurerstrasse 190, CH-8057 Zurich, Switzerland*
† Electronic supplementary information (ESI) available. See DOI: https://doi.org/10.1039/d3lc00817g

This journal is © The Royal Society of Chemistry 2024

slender bodies like *C. elegans* (~600–1000 μm)[53,54] and zebrafish (~1–5 mm).[55–58] Such methods are also strictly limited to rotational instability, bubble collapse, size mismatch, the requirement for a confined operation space, overheating from dissipated acoustic energy, complex instruments, time-consuming, and expensive fabrication. There is still a need for a biologically safe, easy-to-fabricate, easy-to-operate, and high-efficient manipulation method for small model organisms.

Here, we designed an acoustofluidic micromanipulation system for rapid trapping, high-speed rotation, multi-angle imaging, and 3D model reconstruction of zebrafish larvae. The vibrating capillary produces asymmetric acoustic forces and polarized streaming vortices to effectively trap and rotate the zebrafish larva. As a new mechanism, our zebrafish rotating method gives its capacities for ultrafast actuation responses, stable rotation, high-throughput manipulation, safe operation at moderate levels of acoustic pressure, avoiding overheating, easy-to-operate, and portable setup.

We then expanded our research to examine the flow dynamics within the open liquid channel, exploring the effects of varying capillary vibrations, capillary positioning, and the channel's cross-sectional geometry. Our experimental findings, alongside simulations, confirmed the underlying rotational mechanism and offered a deeper understanding of how channel shape influences flow patterns. By tuning the ultrasound excitation voltage, we demonstrated the precisely controlled manipulation of zebrafish larvae. Finally, to showcase its applicability in biological studies, we successfully executed rotational manipulation on fluorescently labeled zebrafish larvae enabling detailed cellular examination, and conducted 3D reconstructions to investigate their morphological characteristics. Given the importance of animal-on-chip

technologies for studying small model animals, our method is expected to become a pivotal tool with diverse applications across the biological and engineering disciplines.

Rotational mechanism

### Polarized vortices induced by a vibrating glass capillary

The acoustofluidic micromanipulation system consists of an acoustofluidic device and an open fluidic channel array, illustrated in Fig. 1 and Video S1.† For the acoustofluidic device, a piezoelectric transducer (PZT) is bonded on a glass capillary, which possesses a pre-pulled sharp tip (Fig. 1c). During experiments, the capillary is horizontally aligned and is positioned close to the channel boundary with its tip submerged into one of the cylindrical liquid channels (Fig. S1, ESI†). When the transducer is excited with a high-frequency square wave signal, ultrasound waves generate and propagate through the capillary, causing it to periodically vibrate. We recorded and analyzed the vibration amplitude of the capillary tip in both air and liquid (Fig. S2, ESI†). When keeping the ultrasound excitation voltage constant, the vibrating amplitude in liquid is weaker than that in air. Due to the acoustofluidic interaction, the vibrating capillary generates polarized acoustic streaming in the surrounding liquid that features the out-of-plane vortex along the long axis of the capillary and the in-plane vortex around the capillary tip, as shown in Fig. 2.

Microparticles placed in an acoustofluidic field predominantly experience both the acoustic radiation force (ARF) and streaming force.[59] Based on the gradient of the Gor'kov potential,[60] the time-averaged ARF acting on a single isolated incompressible particle can be expressed as
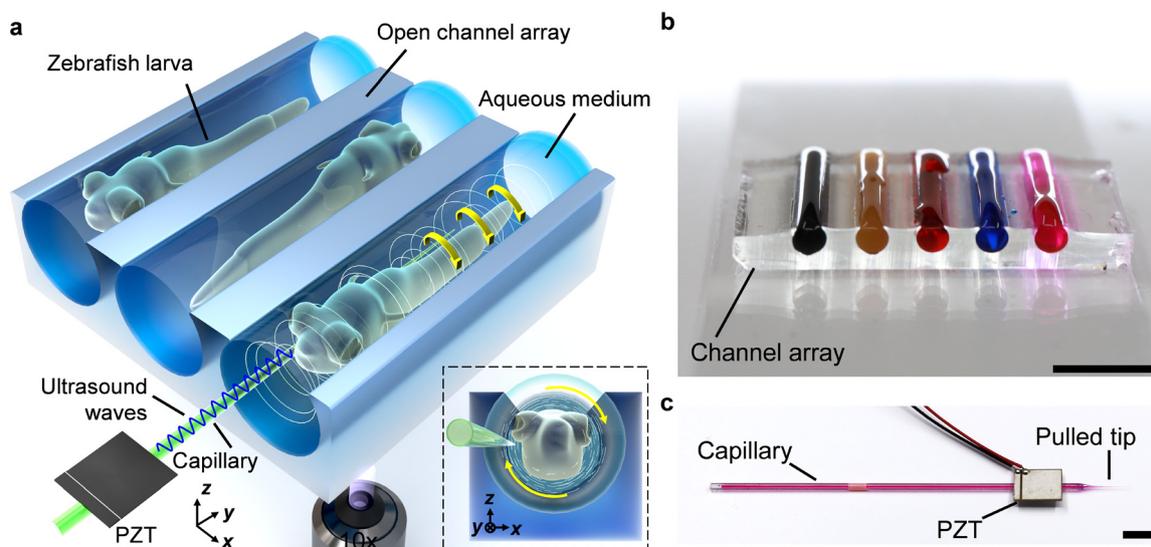
Fig. 1 Acoustofluidic micromanipulation system for zebrafish larvae. a) Illustration of the system consisting of an acoustofluidic device and a liquid-filled open channel array. The inset shows rotation of a zebrafish larva from a cross-sectional perspective. b) The channel array represented by water stained with various colors. Scale bar, 5 mm. c) Feature of the acoustofluidic device, where a piezoelectric transducer is bonded on a glass capillary represented by water stained magenta. Scale bar, 5 mm.
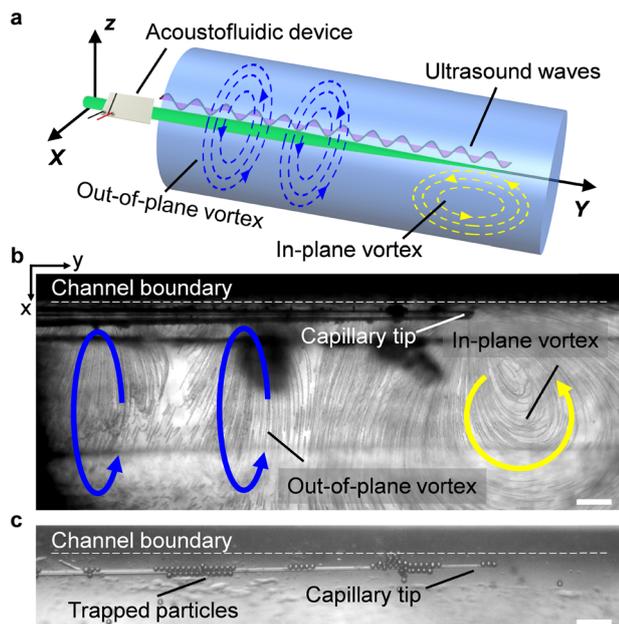
Fig. 2 Acoustofluidic behavior of the vibrating capillary in an open liquid channel. a) Schematic of the polarized vortex. Blue and yellow curved arrows denote the out-of-plane vortex and in-plane vortex, respectively. b) Visualization of both the out-of-plane vortex and in-plane vortex using 2 μm polystyrene particles. The ultrasound excitation frequency and voltage were 185 kHz and 4 V_{PP}, respectively. c) Trapping of 15 μm polystyrene particles around the capillary in liquid. The ultrasound excitation frequency and voltage were 185 kHz and 6 V_{PP}, respectively. Scale bar, 100 μm.

$$F_{AR} = -\frac{4\pi}{3}a^3\nabla\left[f_1\frac{1}{2\rho_0 c_0^2}\langle p_{in}^2\rangle - f_2\frac{3}{4}\rho_0\langle v_{in}^2\rangle\right], \quad (1)$$

$$f_1 = 1 - \tilde{k}, \quad \text{with} \quad \tilde{k} = \frac{k_p}{k_0}, \quad (2)$$

$$f_2 = \frac{2(\tilde{\rho}-1)}{2\tilde{\rho}+1}, \quad \text{with} \quad \tilde{\rho} = \frac{\rho_p}{\rho_0}, \quad (3)$$

where a, p_{in}, and v_{in} are the radius of the particle, incident acoustic pressure, and incident acoustic velocity, respectively; f_1 and f_2 are dimensionless scattering coefficients; ρ_0 and ρ_p respectively denote the density of the liquid and particle; and κ_0 and κ_p denote the compressibility of the liquid and particle, respectively.

The force arising from acoustic streaming can be estimated by the Stokes' drag

$$F_{AS} = 6\pi\eta au, \quad (4)$$

where η is the dynamic viscosity of the liquid and u is the particle velocity. According to eqn (1) and (4), the ARF scales with the particle volume, while the streaming force scales linearly with its radius. Therefore, a particle's motion is determined by the ratio of the two forces

$$\alpha = \frac{F_{AR}}{F_{AS}} \propto a^2\eta^{-1}. \quad (5)$$

For smaller particles, $\alpha \ll 1$, F_{AS} dominates; thus, they follow the streamlines of the vortex. For larger particles, $\alpha \geq 1$, F_{AR} dominates, and this condition allows trapping particles near the capillary. We experimentally verified the behavior of particles with different sizes, as shown in Fig. 2 and Video S2.† 2 μm and 6 μm particles follow the streamlines when the ultrasound field is developed; whereas 10 μm and 15 μm particles are ultimately trapped around the boundary of the capillary, suggesting a size threshold around 6–10 μm, which is much smaller than zebrafish larvae. Further increases in particle size (causing $\alpha \gg 1$), Both the acoustic forces become largely asymmetry on the particle as the acoustic pressure decreases against the propagating distance. Since zebrafish larvae have slender and asymmetrical bodies on the order of thousands of micrometers, a resultant torque will be developed to rotate the larvae.

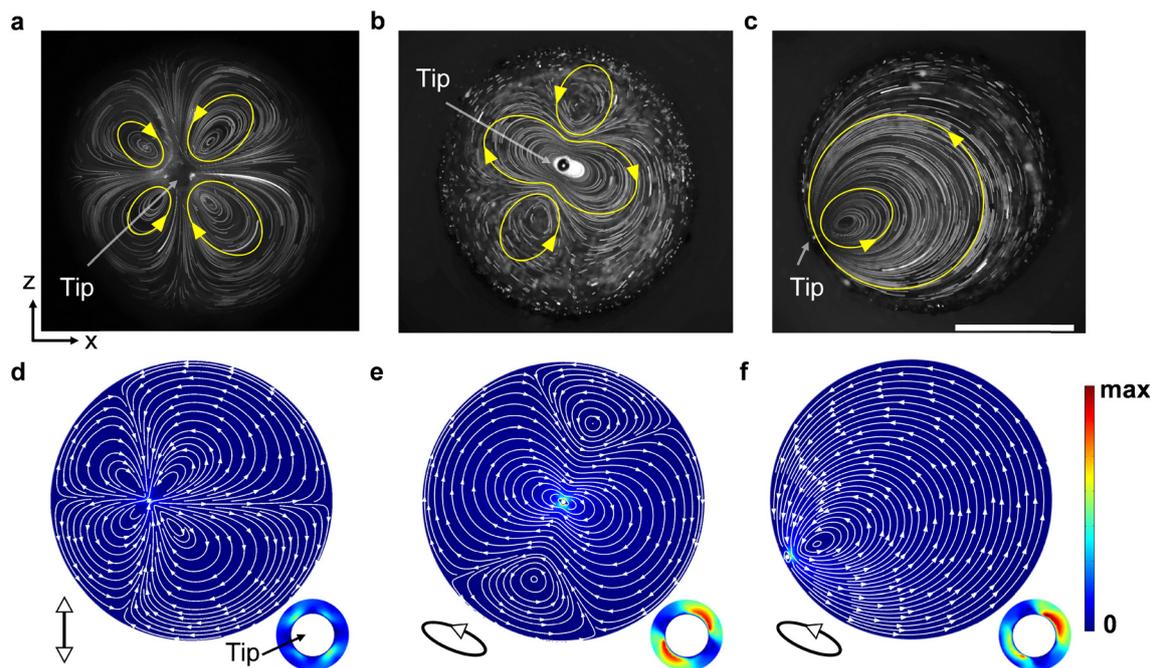### Cross-section flow profile analysis

To gain further insights into the rotational mechanism, we visualized the flow profile through the cross-sectional perspective, (*i.e.*, from the *xz* plane). The acoustofluidic device was held vertically and the tip of the capillary was submerged into the liquid in a cylindrical channel with a consistent inner diameter (1.14 mm) as the open liquid channel used above. The flow profile was observed and recorded from beneath *via* an inverted microscope, as shown in Fig. 3. We then analyzed the generated acoustic streaming by ImageJ.[61]

Fig. 4 shows that when the capillary is excited with different ultrasound excitation frequencies or placed at different positions in the channel, various flow profiles can be developed in the channel. Firstly, as the tip of the capillary was sited near the channel center, we observed two different flow profiles. When the ultrasound excitation frequency was 240 kHz (the natural frequency of the utilized transducer), four in-plane vortices were generated around the tip (Fig. 4a
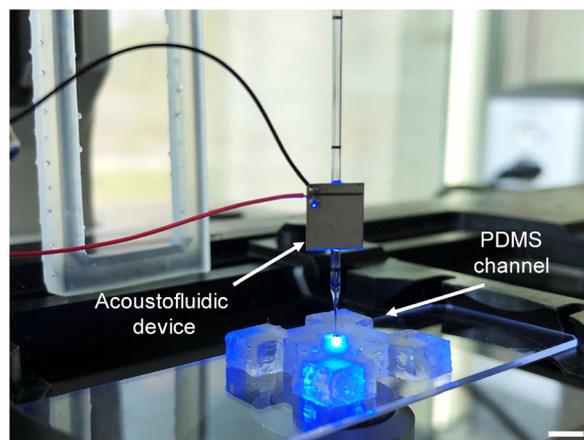
Fig. 3 Experimental setup for cross-section flow profile analysis. Scale bar, 5 mm.

Fig. 4 Experimental and simulated flow profiles viewed in cross-section. a) Flow profile developed with ultrasound excitation frequency at 240 kHz. b) Flow profile developed with ultrasound excitation frequency at 185 kHz. In both profiles, the glass capillary was placed near the center of the channel. c) Flow profile developed with the ultrasound excitation frequency at 185 kHz and the glass capillary placed close to the channel boundary. The ultrasound excitation voltage was kept at 1 V_{PP}. Yellow curves show the developed streaming. Scale bar, 500 μm. d) Flow profile simulation in linear vibrating mode. e) Flow profile simulation in elliptical vibrating mode. f) Flow profile simulation in elliptical vibrating mode with the capillary near the channel boundary. White curves show the developed streaming, while the arrow shows streaming direction and the background color denotes streaming velocity. The vibrating magnitude of the capillary tip was set at 1 nm. Diagrams demonstrate the vibrating mode and direction. Insets show a zoomed-in view of the capillary tips.

and Video S3†); on the other hand, at 185 kHz, three vortices were observed, with one larger vortex rotating around the tip (Fig. 4b). Accordingly, we hypothesize that the variable flow profile is due to the distinct vibrating modes of the capillary tip induced by different ultrasound excitation frequencies: linear vibration in the normal direction and elliptical vibration. Based on theories described in ref. 48 different vibrating modes are caused by complex vibrational coupling between the transducer and capillary. When the exciting frequency of the transducer is far from the natural frequency of the capillary, the transducer prompts the glass capillary to vibrate along the normal direction, and the entire device is linear vibration. However, if the frequency is close to the capillary's natural frequency, the resonance of the entire acoustofluidic device increases significantly, resulting in an elliptical vibration with the oscillation amplitude in the normal direction greater than that in the tangential direction.

To verify the hypothesis, we developed a numerical simulation model to estimate the natural frequency of the utilized glass capillary (see Numerical simulation for configuration details). Simulations of a 50 mm-length capillary without pulling show that its first-order to eight-order natural frequencies are in the range of 453.65 Hz to 52.331 kHz, which is totally out of the operational frequency range in this work. Thus, with the operation frequencies used in this work, the

vibration of the bulk capillary body is negligible in simulations. Then, we simplified the model of the capillary tip without the bulky body (Fig. S3, ESI†). Simulations show that the used excitation frequency, 185 kHz, is close to the 5th-order natural frequency of the capillary tip, verifying the proposed hypothesis.

Next, by keeping the ultrasound excitation frequency at 185 kHz and moving the tip closer to the channel boundary, we observed that those vortices near the boundary decrease in size, and a single vortex becomes dominant across the whole channel (Fig. 4c). This phenomenon is attributable to the no-slip condition of the channel boundary induces asymmetric fluid body forces. We further developed a two-dimensional simulation model to verify this hypothesis (see Numerical simulation for configuration details). In the model, the diameter of the liquid domain was set as 1.14 mm and the tip of the capillary was defined as a circle with a diameter of 20 μm. Fig. 4d–f show that the simulated streamlines coincide with the experimental results. The simulations additionally show that by adjusting the direction of capillary vibration and the distance between the capillary and the boundary, a single polarized vortex in the channel can be generated with multiple vibrating modes (Fig. S4, ESI†), suggesting a good compliance.

Then, to optimize the channel design, we developed different channel types with various cross-section shapes in the simulation model, namely square-, triangle-, and droplet-

shaped channels (with similar dimensions to experimental channels). We found that by placing the vibrating capillary near the channel boundary, a single polarized vortex can be developed in all the simulated channels (Fig. S5, ESI†). We further calculated the streaming velocity of the liquid in the middle of each channel along the z-axis. As depicted in Fig. S5e,† the streaming velocity starts from zero and rapidly increases to maximum over a short z-distance (0–~3 μm). This is because the capillary boundary is also set as a no-slip wall. As the distance from the capillary increases, the streaming velocity decreases to nearly zero, with a large slope (i.e., over ~3 μm to ~150 μm). It is given that acoustic energy attenuates as propagation distance increases. However, the streaming velocity has a small but notable increase at an intermediate distance (~150–~200 μm), which is expected from the dampening effect of the bulk liquid. Finally, the streaming velocity decreases gradually to zero (~200–~1100 μm). The streaming velocity gradient implies the asymmetrical body force in the liquid along the z-axis. As the channel with a circular cross-section featured streaming velocity at a stable amplitude over a large area and by considering the size of zebrafish larvae, the complexity of

channel fabrication, and the observation view, we selected the circular cross-section to demonstrate the manipulation of zebrafish larvae.

Results and discussion

With the designed acoustofluidic manipulation system, we demonstrated the trapping and out-of-plane rotation on living zebrafish larvae, as illustrated in Fig. 5a and b. Firstly, a 4 dpf zebrafish larva anesthetized with sedatives was placed with a pipette into an open channel filled with deionized water. Upon exciting the transducer with the ultrasound excitation frequency of 185 kHz and excitation voltage of 12 V_{PP}, the zebrafish larva was trapped around the capillary tip, as shown in Fig. 5c (where a zebrafish larva slides along the capillary to the tip) and Fig. 5d (where a larva initially in front of the capillary tip was trapped toward it) (Video S4†). The larva can be trapped in 0.1–1 s based on the applied ultrasound excitation voltage. During the process of trapping, the larva began out-of-plane rotation as demonstrated in Fig. 5e and Video S5.† Optical images of the larva from multiple view angles can thus be readily captured.
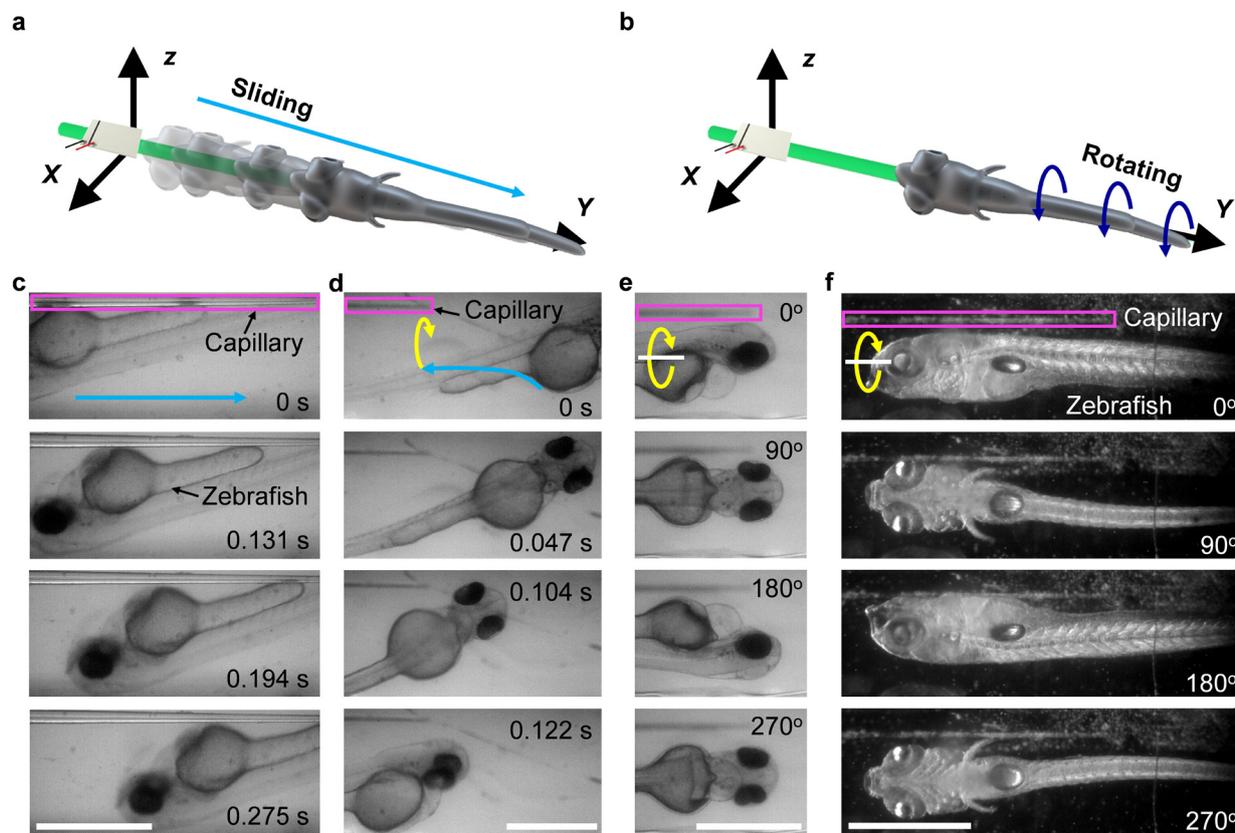
Fig. 5 Trapping and rotation of zebrafish larvae. a) Schematic of zebrafish trapping. b) Schematic of zebrafish rotation. c) A zebrafish larva is trapped and slides down the glass capillary toward the tip. d) A zebrafish larva in front of the capillary is trapped and slides toward the tip. The light-blue lines denote the trajectories of the trapped zebrafish larvae. e) Multiple view angles of a rotating 4 dpf zebrafish larva. Ultrasound excitation frequency and voltage were 185 kHz and 12 V_{PP}, respectively. f) Multiple view angles of a rotating 8 dpf zebrafish larva. Ultrasound excitation frequency and voltage were 185 kHz and 15 V_{PP}, respectively. Yellow curves show the rotating directions. The magenta box denotes the vibrating capillary. Scale bar, 500 μm.

This finding suggests that both the vortices in the liquid (shown in Fig. 2b) contribute to the trapping and rotation of the zebrafish larva; to be specific, the in-plane vortex traps the larva while the out-of-plane vortex rotates it. The calculation of acoustic forces acting on a zebrafish larva is discussed in the ESI† Note. We further demonstrated that an 8 dpf zebrafish larva, which has a bigger swimming bladder and is larger than the 4 dpf larva, was also continuously rotated (Fig. 5f). More than 40 zebrafish larvae of 2–10 dpf with lengths of 700–1200 μm and diameters of 200–300 μm were used to test the stability and repeatability of the system. They were arbitrarily placed into the microchannel and all of them showed stable rotation independent of the orientation, size, and age.

In the experimental domain, the highest Reynolds number was achieved around the capillary tip and was estimated as 50.16 based on $Re = \rho v_s D/\mu$, where ρ is the density of deionized water, 1000 kg m^{-3}; D is the characteristic diameter of the channel, 1140 μm; v_s is the highest measured velocity of the fluid, 44 mm s^{-1}; and μ is the fluid viscosity, 10^{-3} Pa s. The flow of the rotational system can be assumed to be laminar. We observed that in this low Reynolds number regime, the rotating zebrafish larva comes to a stop instantaneously when the ultrasound field is switched off. Based on ref. 51, the relationship between the drag torque T acting on the zebrafish, the acoustic pressure amplitude P, and the excitation voltage V is $T \propto P^2 \propto V^2$. Therefore, the rotational velocity of the zebrafish larva is tunable by changing the ultrasound excitation voltage applied to the transducer. As shown in Fig. 6, effective rotation can be performed at a low voltage, ~5 V$_{PP}$. The rotational velocity increases quadratically with the excitation voltage (where the power function fitting curve has a slope of 2.4); the highest rotational velocity achieved here was ~1080 revolutions per minute (rpm) with an excitation voltage of 20 V$_{PP}$ and excitation frequency of 185 kHz. Notably, the rotational performance and efficiency are affected by multiple factors, including the diameter of the capillary tip, the position of the transducer, and the amount of liquid.

During experiments, we measured the temperature around the zebrafish larva. As depicted in Fig. S6,† the temperature of the liquid did not show a noticeable change before and during acoustofluidic actuation, which is conducive to avoiding overheating that may hurt the biological specimen. We also tested the viability of the rotated zebrafish larvae, as shown in Fig. 7. The larvae that were continuously rotated with a moderate rotational speed for 30 seconds, 1 minute, 5 minutes, and 10 minutes, respectively, had a similar heart rate (90–130 bpm) and blood flow to those grown in E3 medium, implying that the moderate ultrasound treatment and rotation did not harm them. In addition, however, if the ultrasound excitation voltage is ≥20 V$_{PP}$, the lava is at risk of being crushed by large shear forces, as shown in Video S6.† In addition, we operated the zebrafish larvae without a sedative, and they can also be trapped and rotated (Video S6†), implying that a sedative is not necessary for the rotational manipulation. However, without a sedative, the larvae do have the ability and consciousness to escape from the vortex. We envision this phenomenon may open up possibilities for studying stress responses in zebrafish.

To further demonstrate the potential of our acoustofluidic device for zebrafish-based biological applications, we performed rotation manipulation on three types of fluorescently labeled zebrafish larvae (Video S7†). As shown in Fig. 8a, through rotating manipulation, we visualized the distribution of blood vessels through the *kdrl:GFP* transgenic zebrafish larva from multiple view angles. Fig. 8b shows the
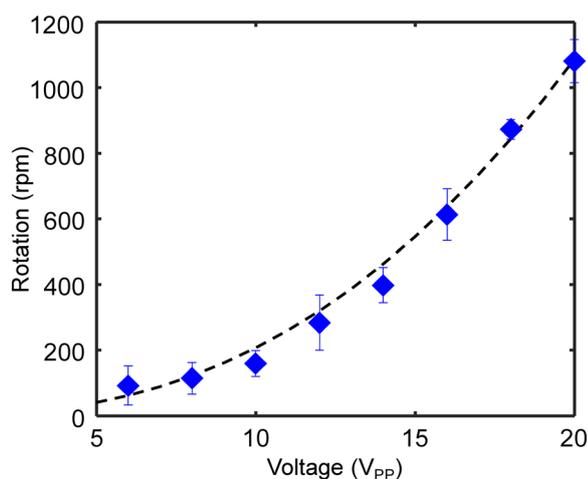

Fig. 6 Plot of the rotational velocity of zebrafish larvae against ultrasound excitation voltage. The ultrasound excitation frequency was kept at 185 kHz. The black dotted curve denotes the fitting with the power function expression, $y = 0.8199x^{2.4}$. The error bars indicate the standard error of the data.
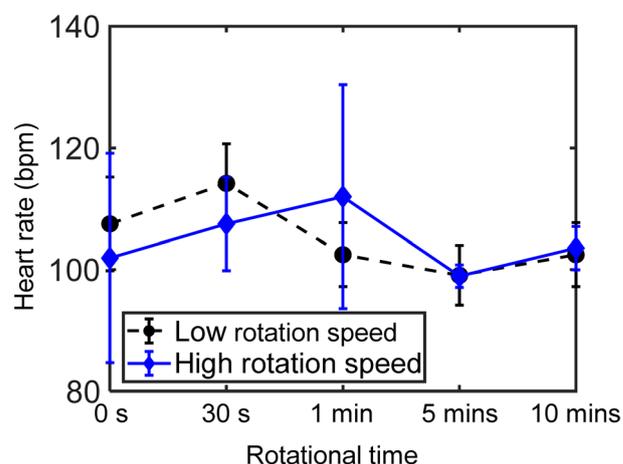

Fig. 7 Viability of the rotated zebrafish larvae *versus* rotational time. The black dotted line denotes the larvae experiencing a low rotational velocity ranging from 150 to 250 rpm; the blue line denotes the larvae experiencing a higher rotational velocity ranging from 400 to 800 rpm. The ultrasound excitation frequency was kept at 185 kHz. More than 30 2–4 dpf zebrafish larvae were studied. The error bars indicate the standard error of the data.
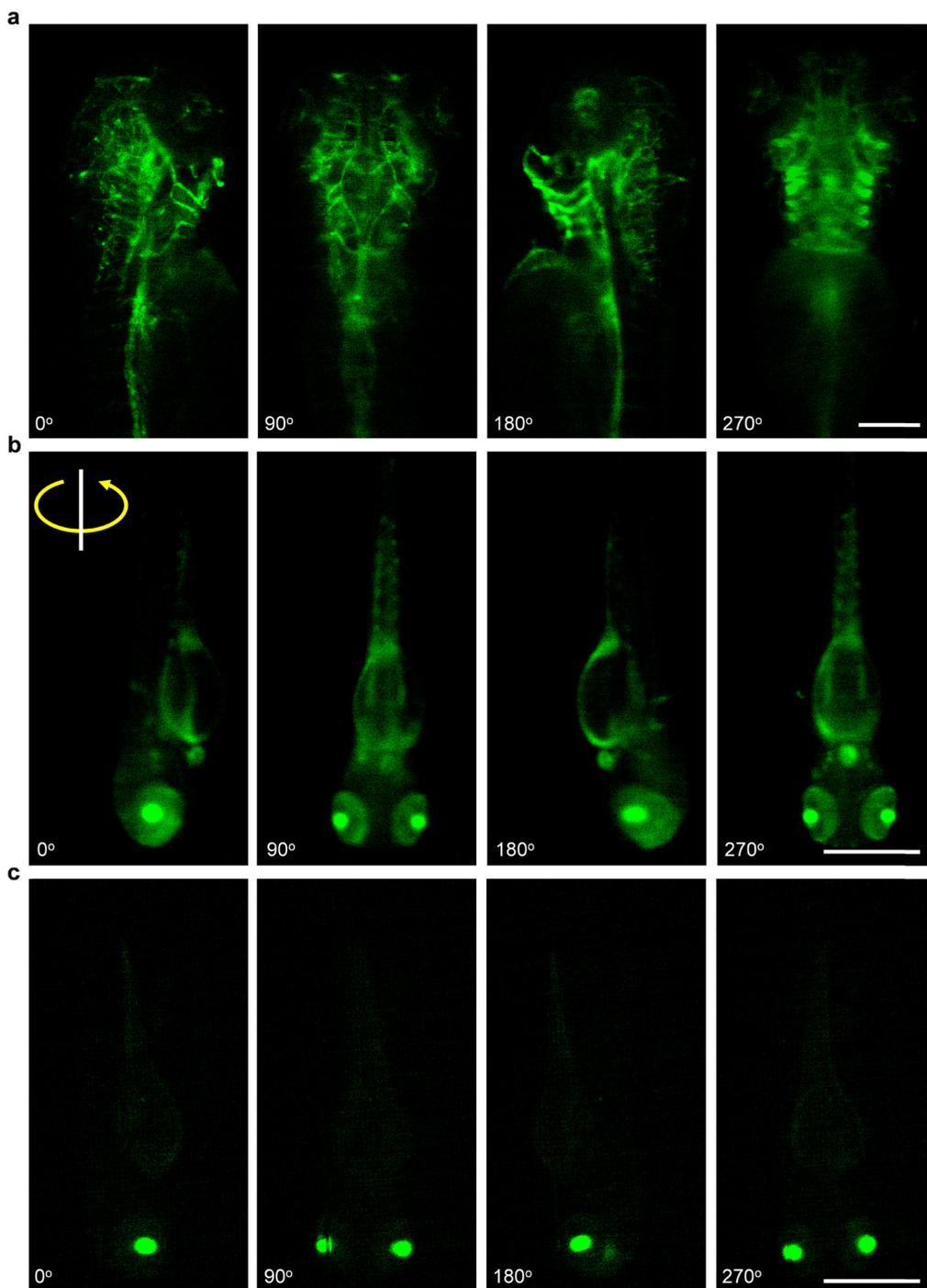
Fig. 8 Multiple view angles of fluorescently labeled zebrafish larvae. a) Blood vessel distribution in a *kdrl:GFP* zebrafish larva. Scale bar, 100 μm. b) The morphology of a *prox1a > Lyn-Citrine; cmlc2:GFP zebrafish* larva. Scale bar, 300 μm. c) The rotating profile of eyes of a zebrafish larva positive for *alpha-crystallin:YFP*. Scale bar, 300 μm.

prox1a > Lyn-Citrine; *cmlc2:GFP* transgenic zebrafish larva with its heart, eyes, brain, and spinal cord fluorescently labeled. During rotation, we can observe the entire profile of the heart and its beating. Notably, also distinct neuronal subpopulations in the retina are visualizable. Fig. 8c shows the rotational image sequences of the fluorescently labeled eyes of an *alpha-crystallin:YFP* transgenic zebrafish larva. We

further studied the 3D distribution of the brain endothelial cells and distinct neurons of the *kdrl:GFP* zebrafish larva. As shown in Fig. 9, the larva was precisely rotated to the target angles in turn and at each pose, we adjusted the focus of the microscope from bottom to up to observe the intricate vasculature distribution in the zebrafish brain slice by slice. We believe our method is promising and useful for zebrafish
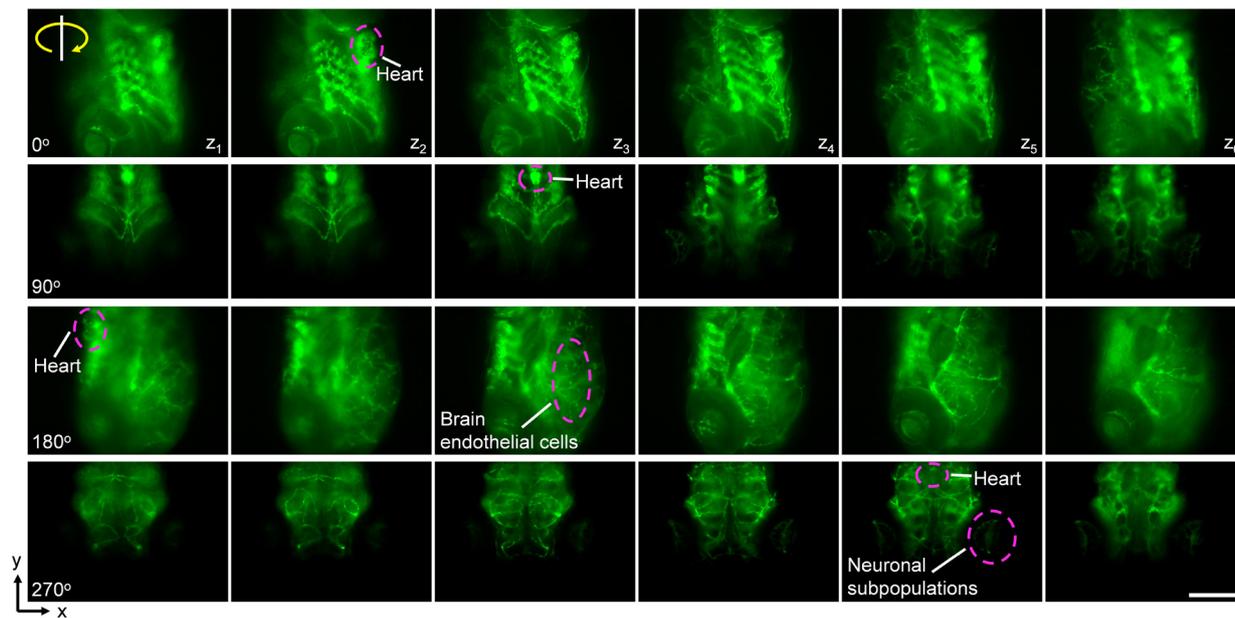
Fig. 9 3D visualization of the fluorescently labeled blood vasculature and neurons. The label of z_i denotes the focus plane of the microscope from bottom to up. Scale bar, 100 μm.

morphological studies, organ analysis, tissue investigations, and interrogations at the cellular level.

The controllable out-of-plane rotation of zebrafish larvae empowers exciting 3D reconstruction from the captured multi-view 2D image sequences. We first collected images of the zebrafish larva from different view angles during several rotation cycles. Imaging preprocesses, including removing noise, enhancing contrast, and adjusting brightness and sharpness were performed to improve the image quality. Subsequently, a feature-based alignment algorithm[62,63] was used to align images by identifying common features, such as corners and edges. The aligned images are then used to
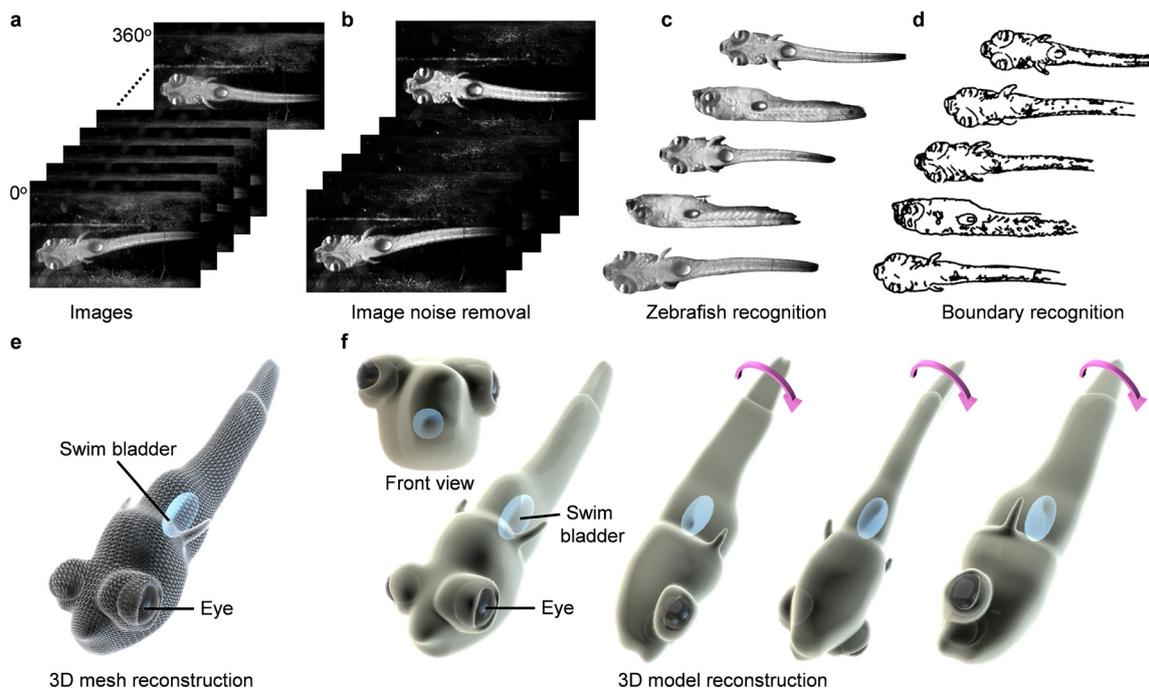

Fig. 10 3D reconstruction of a zebrafish larva. a) Multi-view 2D images captured during rotation manipulation. b) Filtering of recorded images to remove noise. c) Detected zebrafish larva by removing the background. d) Identifying the boundaries of the zebrafish larva at different angles and matching them together. e) Reconstruction of a 3D model using point clouds and joining the points with triangular elements. f) A rendered reconstructed 3D model of the zebrafish larva.

reconstruct a point cloud of the larva using a process called stereo matching.[64] The point cloud is further converted into a mesh by connecting the points in a triangular pattern. By averaging the positions of the points in the mesh, the mesh is smoothed to remove sharp edges or artifacts. A hole-filling process is then used to fill the holes in the mesh.[65] Fig. 10 shows such an example rendering from the 3D mesh with a visualized ellipsoidal swim bladder inside the larva (Video S8†). 3D reconstruction of other internal organs (heart, liver, bone, *etc.*) of zebrafish larvae is challenging and suffers from problems such as being off the axis of rotation, small size, occluded by other objects, and out of focus at certain viewing angles. Increasing the camera's frame rate, reducing the rotation speed, and optimizing geometric parameters of the channel can reveal more detailed information about the larvae.

Currently, confocal imaging and light-sheet imaging can perform 3D imaging and 3D reconstruction with a high resolution. However, the focus range of confocal imaging is narrow, which makes it difficult to scan the whole structure with a single view and requires a long operation time. Light-sheet imaging is much faster than confocal imaging by using a plane of light instead of a point. But this method is also difficult for high-throughput imaging. The 3D reconstruction through these machines could also have imaging distortion, for example, a sphere may be reconstructed as an ellipsoid. These machines are hard to integrate into other systems for comprehensive analysis. Additionally, these machines are expensive and not accessible to all labs. By contrast, our system offers the following advantages: (i) our platform allows fast 3D imaging of the whole zebrafish larva, which could be captured within milliseconds; (ii) our platform could enable high-throughput imaging by simultaneously rotating multiple zebrafish larvae; (iii) our system is miniaturized, portable, and adaptable for integration with other operation systems, for example, microfluidic devices and microinjection probes; (iv) our system has a high cost-effective. For a single chip, the cost is around 10 dollars.

Conclusions

An accurate system for positioning and rotating zebrafish larvae is a powerful and fundamental tool for further biomedical manipulation of this vertebrate model organism. In this work, we designed an on-chip acoustofluidic micromanipulation system. The acoustofluidic device induces asymmetrical forces into the surrounding liquid. By controlling the polarized vortices thus generated, we demonstrated fast trapping and high-speed rotation of zebrafish larvae around the capillary tip. Simulations of cross-sectional flow profiles were consistent with the experimental results, which verified the mechanism of the polarized vortex, and provided insights into the effects of channel geometry. Compared to existing methods, our acoustofluidic system provides a fast and inexpensive approach to manipulating and observing small living organisms without complex sample preparation and setup. The open channel

allows further sophisticated contact manipulation. Since acoustic energy is not directly leaked into the liquid, overheating during operation is avoided. Most importantly, our portable manipulation system allows array expansion for high-throughput manipulation. It is expected that the sequence operation can be developed to operate larvae one by one; the channel and capillary can also be facilely copied to parallelly operate multiple larvae in one batch. A high rotational speed can accelerate the imaging and analysis process, which also has the potential for high-throughput manipulation. Additionally, it could become a new tool to capture the dynamic response of zebrafish larvae, for example, the blood flow, heart beating, drug metabolism, neuron response, and so on. With its superior performance and general applicability, we demonstrated the 3D visualization of fluorescently labeled neurons and vasculature distribution of zebrafish larvae. We further performed 3D reconstruction of the larvae, suggesting our acoustofluidic micromanipulation system will be a valuable tool for diverse studies in model organisms. In the future, we will explore more zebrafish-based biomedical applications of the system, including 3D mechanical characterization, surface detection, micro-injection, drug screening, Immune response, neural linking, and more; and optimize the channel properties for precise manipulation of small organisms on different scales.

To characterize the resolution of our technique, we observed the blood cells (with a diameter of ~8 μm) of the rotating zebrafish. As shown in Fig. S7,† with the 10× objective, a high-speed camera (3030 frames per second), and a lower rotational velocity, 0–100 rpm, the blood cells in the larva's vessels are clearly observed without a fluorescent label. Based on the experiment results, we believe our technique is valuable for cell-level zebrafish studies. The imaging resolution could be further improved using ultra-high-speed and ultra-high-sensitive cameras.

Materials and method

Device design and fabrication

For the acoustofluidic device, glass capillaries with a diameter of 1.14 mm were first pulled using a micropipette puller. The tip of the pulled capillary is then broken manually with a diameter of 20 ± 8 μm for a stable flow field. A rectangular piezoelectric transducer with dimensions 7.0 × 8.0 × 0.2 mm (Steminc, USA) was bonded using a two-component epoxy (UHU Plus Sofortfest) to the pulled capillary at 5 mm from the end of the tip. To produce the open channel, polydimethylsiloxane (PDMS) resin (mixed with a curing agent at a 10 : 1 ratio) was poured into a chassis that was 3D printed out of black photopolymer resin (Form3, FormLabs), and then a glass capillary was submerged ~80 percent into the mixture from the top. After curing, the PDMS substrate was lifted away. The cross-sectional area of the microchannel is 80% of a circle with a diameter of 1.14 mm, and the channel length is 8 mm. For rotation operations, the PDMS channel was first bonded onto a glass slide by oxygen plasma treatment. Then, to ensure precise positioning of the capillary in the channel, a 3D-printed casing

was used to mount the acoustofluidic device on the glass slide. The casing allows the fast replacement of the capillary between channels. Channels for the cross-section flow profile study were fabricated by the same method. During experiments, the transducer is excited with a high-frequency square wave signal generated by a function generator (0–25 MHz, 0–10 V_{pp}, Tektronix AFG1022, Tektronix, Inc., USA) and an amplifier (0–60 V_{pp}, 15× amplification, High Wave 3.2v, Digitum-Elektronik).

Zebrafish larvae preparation

Zebrafish larvae (2–10 dpf) were used to show the rotation operation. Zebrafish strain were kept in a 14 h/10 h light/dark cycle under standard conditions. To avoid unwanted movement during experiments, zebrafish larvae were paralyzed with a sedative (3-amino-benzoic acid ethyl ester (MS-222, tricaine, MESAB; Sigma Aldrich) at 0.01% from pH 7.0 bicarbonate buffered stock solution) in an E3 medium (5 mM NaCl, 0.17 mM KCl, 0.33 mM CaCl$_2$, and 0.33 mM MgSO$_4$) at 26 °C. The following fluorescent lines were used: *tg(kdrl:EGFP)^{s843}*,[66] *TgBAC(prox1a:KALTA4, 4xUAS-E1B:TagRFP)^{nim5}*, *Tg(5xUAS-E1B:LY-Citrine, cryaa:Citrine)^{nim23}*,[67] *Tg(hsp70l:GFP-RAB11a, cmlc2: GFP)^{pd1031}*.[68] Three day-old larvae were pre-screened for the presence of transgenes of interest using a fluorescence stereomicroscope (Olympus).

Numerical simulation

Numerical simulations were conducted using the commercial COMSOL Multiphysics software (v5.6, Burlington, MA). For the natural frequency study, the material of the capillary tip is solid glass (a built-in material in COMSOL). The inner and outer diameters of the capillary are 1.14 mm and 0.2 mm, respectively. The length of the capillary tip is 8 mm, and the minimum diameter of the tip is 20 μm. For the cross-section flow profile study, we performed ultrasound vibration of the capillary with the "thermoviscous acoustics, frequency domain" physical field. The "laminar flow" physical field was used to denote the liquid domain. The "no-slip" condition was used to set boundaries. The physics-controlled mesh was utilized. Other parameters and configuration used in numerical simulations are listed in Table S1.†

Imaging and data analysis

The rotation system was mounted on an inverted microscope (Axiovert 200 M, Zeiss). Videos were recorded with a high-speed camera (Chronos 1.4, Kron Technologies) and then analyzed in ImageJ.

Live subject statement

All experiments were conducted in accordance with local authorities (Zürich Switzerland: Kantonales Veterinäramt TV4206).

Author contributions

Conflicts of interest

There are no conflicts of interest to declare.

Acknowledgements

References

1 M. B. Orger and G. G. De Polavieja, *Annu. Rev. Neurosci.*, 2017, **40**, 125.

2 R. Dahm and R. Geisler, *Mar. Biotechnol.*, 2006, **8**, 329.

3 K. Liu, C. Petree, T. Requena, P. Varshney and G. K. Varshney, *Front. Cell Dev. Biol.*, 2019, **7**, 1.

4 H. W. Detrich, M. Westerfield and L. I. Zon, *Methods Cell Biol.*, 1999, **59**, 3.

5 C. A. MacRae and R. T. Peterson, *Nat. Rev. Drug Discovery*, 2015, **14**, 721.

6 G. Kari, U. Rodeck and A. P. Dicker, *Clin. Pharmacol. Ther.*, 2007, **82**, 70.

7 H. Feitsma and E. Cuppen, *Mol. Cancer Res.*, 2008, **6**, 685.

8 D. G. Howe, Y. M. Bradford, A. Eagle, D. Fashena, K. Frazer, P. Kalita, P. Mani, R. Martin, S. T. Moxon, H. Paddock, C. Pich, S. Ramachandran, L. Ruzicka, K. Schaper, X. Shao, A. Singer, S. Toro, C. Van Slyke and M. Westerfield, *Nucleic Acids Res.*, 2017, **45**, D758.

9 E. E. Patton, L. I. Zon and D. M. Langenau, *Nat. Rev. Drug Discovery*, 2021, **20**, 611.

10 S. Cassar, I. Adatto, J. L. Freeman, J. T. Gamse, I. Iturria, C. Lawrence, A. Muriana, R. T. Peterson, S. Van Cruchten and L. I. Zon, *Chem. Res. Toxicol.*, 2020, **33**, 95.

11 S. C. Baraban, M. T. Dinday, P. A. Castro, S. Chege, S. Guyenet and M. R. Taylor, *Epilepsia*, 2007, **48**, 1151.

12 Y. Geng and R. T. Peterson, *Zebrafish*, 2021, **18**, 376.

13 L. Lin, X. Peng, X. Wei, Z. Mao, C. Xie and Y. Zheng, *ACS Nano*, 2017, **11**, 3147.

14 J. Li, P. S. Kollipara, Y. Liu, K. Yao, Y. Liu and Y. Zheng, *ACS Nano*, 2022, **16**, 6.

15 I. A. Favre-Bulle, A. B. Stilgoe, H. Rubinsztein-Dunlop and E. K. Scott, *Nat. Commun.*, 2017, **8**, 630.

16 P. Yu, Y. Liu, Q. Zhao, Z. Wang, Y. M. Li and L. Gong, *Appl. Phys. Express*, 2020, **13**, 032008.

17 F. Berndt, G. Shah, R. M. Power, J. Brugués and J. Huisken, *Nat. Commun.*, 2018, **9**, 1.

18 M. F. Yanik, C. B. Rohde and C. Pardo-Martin, *Annu. Rev. Biomed. Eng.*, 2011, **13**, 1.

19 C. Pardo-Martin, T. Y. Chang, B. K. Koo, C. L. Gilleland, S. C. Wasserman and M. F. Yanik, *Nat. Methods*, 2010, **7**, 634.

20 Y. Guo, W. J. Veneman, H. P. Spaink and F. J. Verbeek, *Biomed. Opt. Express*, 2017, **8**, 2611.

21 S. G. Hong, P. Lee, S. C. Baraban and L. P. Lee, *Sci. Rep.*, 2016, **6**, 1.

22 F. Yang, Z. Chen, J. Pan, X. Li, J. Feng and H. Yang, *Biomicrofluidics*, 2011, **5**, 024115.

23 N. M. Fuad, J. Kaslin and D. Wlodkowic, *Biomicrofluidics*, 2017, **11**, 05110.

24 V. M. Jooss, J. S. Bolten, J. Huwyler and D. Ahmed, *Sci. Adv.*, 2022, **8**, 1.

25 P. Agrawal, Z. Zhang, Z. Ghorbanikharaji, Z. Shi and D. Ahmed, *Acoustic field techniques for cell characterization in health monitoring*, Elsevier Inc., 2023.

26 J. Rufo, F. Cai, J. Friend, M. Wiklund and T. J. Huang, *Nat. Rev. Methods Primers*, 2022, **2**, 1.

27 A. Ozcelik, J. Rufo, F. Guo, Y. Gu, P. Li, J. Lata and T. J. Huang, *Nat. Methods*, 2018, **15**, 1021.

28 C. Dillinger, N. Nama and D. Ahmed, *Nat. Commun.*, 2021, **12**, 1–11.

29 Z. Zhang, Z. Shi and D. Ahmed, *arXiv*, 2023, preprint, DOI: 10.48550/arXiv.2307.05754.

30 Y. Deng, A. Paskert, Z. Zhang, R. Wittkowski and D. Ahmed, *Sci. Adv.*, 2023, **9**, eadh526.

31 A. D. C. Fonseca, C. Glück, J. Droux, Y. Ferry, C. Frei, S. Wegener, B. Weber, M. E. Amki and D. Ahmed, *Nat. Commun.*, 2023, **14**, 5889.

32 Z. Zhang, A. Sukhov, J. Harting, P. Malgaretti and D. Ahmed, *Nat. Commun.*, 2022, **13**, 7347.

33 J. Janiak, Y. Li, Y. Ferry, A. A. Doinikov and D. Ahmed, *Nat. Commun.*, 2023, **14**, 4705.

34 J. Rufo, F. Cai, J. Friend, M. Wiklund and T. J. Huang, *Nat. Rev. Methods Primers*, 2022, **2**, 30.

35 P. Zhang, H. Bachman, A. Ozcelik and T. J. Huang, *Annu. Rev. Anal. Chem.*, 2020, **13**, 17–43.

36 Z. Tian, S. Yang, P. Huang, Z. Wang, P. Zhang, Y. Gu, H. Bachman, C. Chen, M. Wu and T. J. Huang, *Sci. Adv.*, 2019, **5**, 5.

37 Q. Zhou, V. Sariola, K. Latifi and V. Liimatainen, *Nat. Commun.*, 2016, **7**, 12764.

38 A. Kopitca, K. Latifi and Q. Zhou, *Sci. Adv.*, 2021, **7**, 39.

39 X. Bai, S. Bin, D. Yuguo, Z. Wei, F. Yanmin, C. Yuanyuan, Z. Deyuan, A. Fumihito and F. Lin, *Sens. Actuators, A*, 2020, **315**, 112340.

40 L. Feng, B. Song, Y. Chen, S. Liang, Y. Dai, Q. Zhou, D. Chen, X. Bai, Y. Feng, Y. Jiang, D. Zhang and F. Arai, *Biomicrofluidics*, 2019, **13**, 064103.

41 E. Kim, M. Kojima, L. Xiaoming, T. Hattori, K. Kamiyama, Y. Mae and T. Arai, *ROBOMECH J.*, 2017, **4**, 5.

42 Y. Li, X. Liu, Q. Huang, A. T. Ohta and T. Arai, *Lab Chip*, 2021, **21**, 1016.

43 X. Liu, Y. Li, L. Li, M. Kojima, Q. Shi, Q. Huang, T. Fukuda and T. Arai, *IEEE/ASME Trans. Mechatron.*, 2022, 3164263.

44 A. Ozcelik, N. Nama, P. H. Huang, M. Kaynak, M. R. McReynolds, W. Hanna-Rose and T. J. Huang, *Small*, 2016, **12**, 5120.

45 Y. Zhou, J. Liu, J. Yan, S. Guo and T. Li, *Small*, 2021, **17**, 1.

46 Q. Tang, F. Liang, L. Huang, P. Zhao and W. Wang, *Biomed. Microdevices*, 2020, **22**, 1.

47 I. Bernard, A. A. Doinikov, P. Marmottant, D. Rabaud, C. Poulain and P. Thibault, *Lab Chip*, 2017, **17**, 2470.

48 X. Liu, Q. Shi, Y. Lin, M. Kojima, Y. Mae, T. Fukuda, Q. Huang and T. Arai, *Small*, 2019, **15**, 1.

49 C. Dai, Y. Sun, L. Xin, Z. Zhang, G. Shan, T. Wang, K. Zhang, X. Wang, L. T. Chu and C. Ru, *IEEE Robot. Autom. Lett.*, 2020, **5**, 339.

50 N. F. Läubli, M. S. Gerlt, A. Wüthrich, R. T. M. Lewis, N. Shamsudhin, U. Kutay, D. Ahmed, J. Dual and B. J. Nelson, *Anal. Chem.*, 2021, **93**, 9760.

51 N. F. Läubli, N. Shamsudhin, H. Vogler, G. Munglani, U. Grossniklaus, D. Ahmed and B. J. Nelson, *Small Methods*, 2019, **3**, 1.

52 N. F. Läubli, J. T. Burri, J. Marquard, H. Vogler, G. Mosca, N. Vertti-Quintero, N. Shamsudhin, A. deMello, U. Grossniklaus, D. Ahmed and B. J. Nelson, *Nat. Commun.*, 2021, **12**, 2583.

53 J. Zhang, S. Yang, C. Chen, J. H. Hartman, P. H. Huang, L. Wang, Z. Tian, P. Zhang, D. Faulkenberry, J. N. Meyer and T. J. Huang, *Lab Chip*, 2019, **19**, 984.

54 D. Ahmed, A. Ozcelik, N. Bojanala, N. Nama, A. Upadhyay, Y. Chen, W. Hanna-Rose and T. J. Huang, *Nat. Commun.*, 2016, **7**, 11085.

55 J. Durrer, P. Agrawal, A. Ozgul, S. C. F. Neuhauss, N. Nama and D. Ahmed, *Nat. Commun.*, 2022, **13**, 6370.

56 C. Chen, Y. Gu, J. Philippe, P. Zhang, H. Bachman, J. Zhang, J. Mai, J. Rufo, J. F. Rawls, E. E. Davis, N. Katsanis and T. J. Huang, *Nat. Commun.*, 2021, **12**, 1118.

57 Z. Chen, X. Liu, X. Tang, Y. Li, D. Liu, Y. Li, Q. Huang and T. Arai, *IEEE Robot. Autom. Lett.*, 2022, **7**, 4.

58 Z. Zhang, L. K. Allegrini, N. Yanagisawa, Y. Deng, S. C. F. Neuhauss and D. Ahmed, *IEEE Robot. Autom. Lett.*, 2023, **8**, 5.

59 D. L. Miller, *J. Acoust. Soc. Am.*, 1988, **84**, 1378.

60 G. Go, J. Han, J. Zhen, S. Zheng, A. Yoo, M. J. Jeon, J. O. Park and S. Park, *Adv. Healthcare Mater.*, 2017, **6**, 1.

61 C. A. Schneider, W. S. Rasband and K. W. Eliceiri, *Nat. Methods*, 2012, **9**, 671.

62 F. Liang, J. Zhu, H. Chai, Y. Feng, P. Zhao, S. Liu, Y. Yang, L. Lin, L. Cao and W. Wang, *Small Methods*, 2023, **7**, 2201492.

63 C. A. Brassey and J. D. Gardiner, *R. Soc. Open Sci.*, 2015, **2**, 150302.

64 L. Huang, Y. Feng, F. Liang, P. Zhao and W. Wang, *Biomicrofluidics*, 2021, **15**, 014106.

65 L. Huang, P. Zhao and W. Wang, *Lab Chip*, 2018, **18**, 2359.

66 D. Beis, T. Bartman, S. W. Jin, I. C. Scott, L. A. D'Amico, E. A. Ober, H. Verkade, J. Frantsve, H. A. Field, A. Wehman, H. Baier, A. Tallafuss, L. Bally-Cuif, J. N. Chen, D. Y. R. Stainier and B. Jungblut, *Development*, 2005, **132**, 4193–4204.

67 J. Cayuso, A. Dzementsei, J. C. Fischer, G. Karemore, S. Caviglia, J. Bartholdson, G. J. Wright and E. A. Ober, *Dev. Cell*, 2016, **39**, 316–328.

68 A. L. Alvers, S. Ryan, P. J. Scherz, J. Huisken and M. Bagnat, *Development*, 2014, **141**, 1110–1119.